VI. MICROWAVE ELECTRONICS*

Prof. L. D. Smullin
Prof. H. A. Haus
Prof. A. Bers
C. G. Alexander
K. Arons
J. Hennel
R. B. McCullough
D. L. Morse
W. D. Rummler
W. K. Rushforth

A. THE X-LINE SLOW-WAVE STRUCTURE

In Quarterly Progress Report No. 56 (pages 104-107) some preliminary measurements performed on an elementary X-line were presented. Detailed measurements have been made on several variations of this structure to ascertain the factors that determine the edges of the lowest passband.

The X-lines that were tested were made from obstacles like that shown in Fig. VI-1, separated by hollow cylindrical spacers. Figure VI-2 is a schematic drawing of an X-line showing the geometric parameters of the structure. The angle a denotes the angular displacement of even-numbered bars with respect to odd-numbered bars.

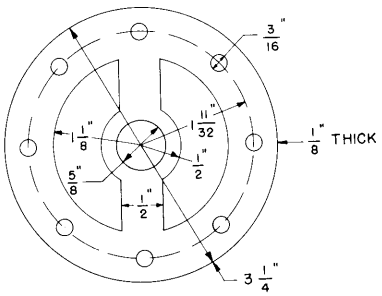

Fig. VI-1. X-line obstacle.

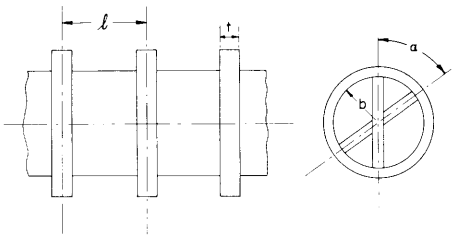

Fig. VI-2. Schematic drawing of the X-line showing geometric parameters.

The ω-β diagrams of several X-lines that were tested were obtained by short-circuiting a section of the periodic structure having a length $N\ell$. For each passband of the structure, this short-circuited line has N + 1 resonant frequencies. The line is resonant when the phase shift per period is

$$\beta_o = \frac{p\pi}{N\ell} \qquad p = 0, 1, 2, \ldots, N \tag{1}$$

The resonances are identified by moving a metallic needle along the axis of the structure (this perturbs only the E_z-field) and counting the number of nodes in the field pattern.

*This work was supported in part by Purchase Order DDL B-00306 with Lincoln Laboratory, a center for research operated by Massachusetts Institute of Technology with the joint support of the U. S. Army, Navy, and Air Force under Air Force Contract AF19(604)-5200.

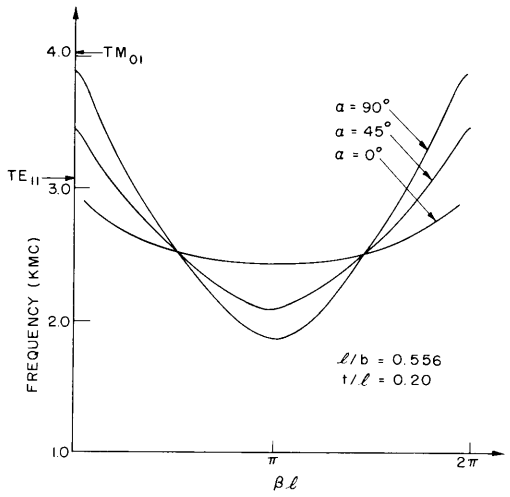

Fig. VI-3. ω-β diagrams for three values of α.

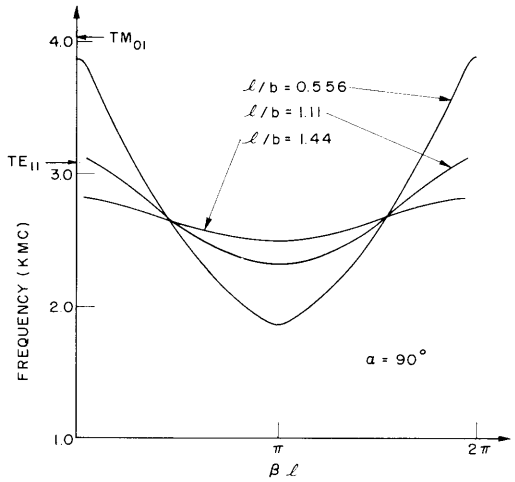

Fig. VI-4. ω-β diagrams for three values of ℓ/b.

The number of nodes is the same as the index p in Eq. 1. Figures VI-3 and VI-4 show the ω-β diagrams that were obtained by this method.

The following explanation of the increased dispersion and wider passband with increased α (Fig. VI-3) is offered. The structure with $\alpha = 0$ could be likened to a mode filter if the bars were closely spaced thin wires instead of thick bars. Such a mode filter would remove the polarization degeneracy of the TE_{11} mode. Hence, for this case, the mode of propagation may be viewed as a slightly perturbed TE_{11} mode with an E-field polarization normal to the bars. A possible justification for this line of reasoning is that the zeroth mode of the resonator does not exist (there is no TE_{110} mode in a circular cylindrical cavity), but the dispersion curve approaches the TE_{11} cutoff as $\beta\ell$ approaches zero.

For the other extreme (α=90°) shown in Fig. VI-3 we may apply a similar line of reasoning. Since adjacent bars are at right angles, and the spacing between the bars is small, no mode resembling a TE_{11} mode is likely to propagate. The upper cutoff frequency in this case is near the TM_{01} cutoff frequency. As the angle α is increased from zero to 90°, the upper band edge moves from near the TE_{11} cutoff to the TM_{01} cutoff.

This same line of reasoning can be used to explain the effect of varying ℓ/b on the upper cutoff frequency (Fig. VI-4). For large ℓ/b we might expect a wave similar to a TE_{11} wave to propagate. As ℓ/b is decreased, the upper cutoff frequency increases and approaches the TM_{01} cutoff, as before.

Another pronounced effect of increasing α is the depression of the lower cutoff frequency. This can best be explained by considering the π resonance, the frequency of which corresponds to the lower cutoff frequency, as a resonance between adjacent wires.

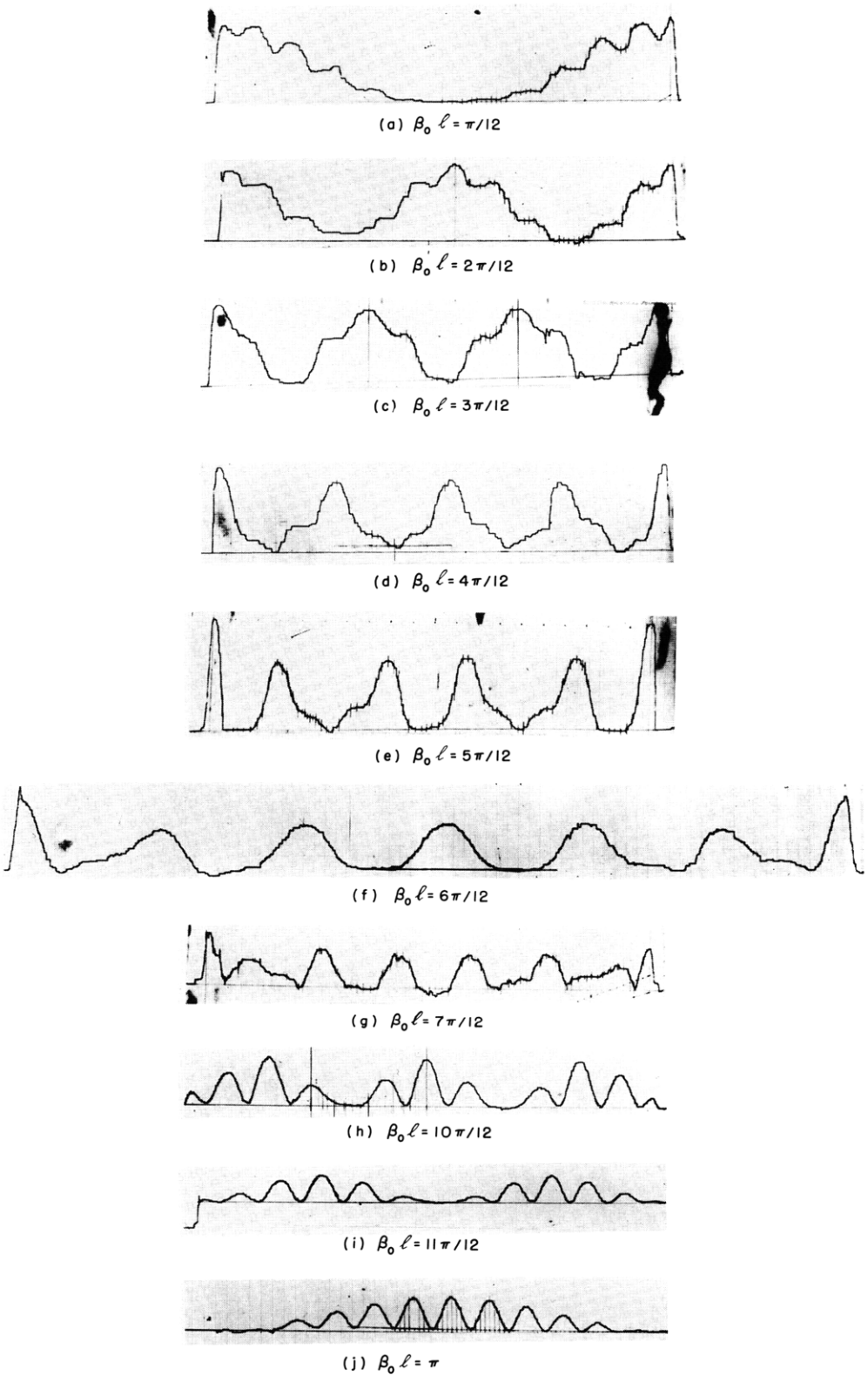

Fig. VI-5. Plots of E_z^2 for a resonated X-line of 12 sections: $\ell/b = 0.556$; $t/\ell = 0.20$; $a = 90°$.

Since the spacing between the bars is small for the case shown in Fig. VI-3, the effect of rotating succeeding bars is that the inductance between the ends of the bars increases more rapidly than the capacitance between the bars decreases.

The decrease in the lower cutoff frequency for decreasing ℓ/b may also be explained in this manner. It is evident that for the range of ℓ/b that was considered the principal effect of reducing ℓ/b is to increase the capacitance between adjacent bars.

It should be noted that the frequency of the "mid-wavelength" resonance ($\beta_o \ell = \pi/2$) is independent of α. This does not seem unreasonable because at this resonance adjacent bars are 90° out of phase and hence are completely uncoupled.

Figure VI-5 shows a plot of the E_z^2 fields on the axis for 10 of the 13 resonances of a 12-cell X-line having $\alpha = 90°$, $\ell/b = 0.556$. Inspection of the resonances for $\beta_o \ell = \pi/12$ to $\beta_o \ell = 7\pi/12$ (Fig. VI-5a-5g) reveals that the square roots of these plots look as they might be expected to look. It can be shown that the E_z-field in a short-circuited section of a periodic structure of length $N\ell$ is given by

$$E_z = \sum_n A_n \cos\left(\beta_o - \frac{2\pi n}{\ell}\right) z \qquad (2)$$

where the β_o for the p^{th} resonance is given by Eq. 1. Each of the plots in Fig. VI-5a-5g is composed of a variation of the form $\cos \beta_o z$ plus a visible harmonic distortion that indicates a variation of the form $\cos (\beta_o - 2\pi/\ell)\, z$.

The E_z^2 field plot in Fig. VI-5h breaks into 3 sections. This plot was assigned a value of β_o in accordance with the number of nodes in the field pattern, but no way has been found to synthesize such a field plot from the terms of the series in Eq. 2. The same statements can be made in regard to the plots of Fig. VI-5i, 5j. The effect that is described above indicates that there is an anomaly in the shape of the ω-β diagram in this region, or that there is another mode of propagation in the structure in this range of frequencies.

A more complete report of the work described here may be found in the author's Master of Science thesis which was submitted to the Department of Electrical Engineering, M. I. T., September 1960.

W. D. Rummler

B. SLOW BACKWARD WAVES IN AN ELECTRON-BEAM WAVEGUIDE

A test has been devised for determining the existence of natural, backward, slow waves in a system consisting of an electron beam drifting through a waveguide. The linearized small-signal approach is used to describe the system. The assumptions used in setting up the model are:

(a) Neutralized electron beam drifting in a waveguide, free of static electric fields, having perfectly conducting walls.

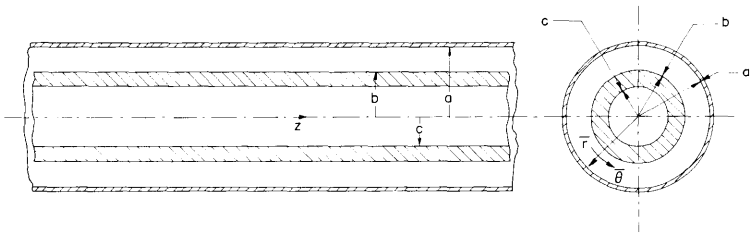

Fig. VI-6. Geometry of the hollow electron-beam system in a circular waveguide.

(b) Infinite magnetic-focusing field oriented in the direction of time-average electron drift.

(c) Uniform, time-average charge and velocity in any plane transverse to the direction of drift.

(d) Single-valued, time-average velocity and density.

The system propagation constants are found by solving the characteristic set of equations (see Hahn (1) and Ramo (2)) for the system:

$$(qb)^2 = (kb)^2 - (\beta b)^2 \tag{1}$$

$$(pb)^2 = \left[(kb)^2-(\beta b)^2\right]\left[1 - \frac{(\beta_p b)^2}{(\beta_e-\beta)^2\, b^2}\right] \tag{2}$$

$$D(pb, qb, a, b, c) = 0 \tag{3}$$

where an $e^{-j\beta z}$ dependence has been assumed for all field quantities. For TM waves in a cylindrical system in which the electron beam and drift tube are concentric, we have

$$D(pb, qb, a, b, c) = \left[\frac{pb}{qb}\right]^2 \left[\frac{J_o(qc)}{J_1(qc)} \cdot \frac{H_{0,0}(qb, qa)\, H_{1,1}(pb, pc)}{H_{1,0}(qb, qa)\, H_{0,0}(pb, pc)}\right]$$
$$- \frac{pb}{qb}\left[\frac{J_o(qc)}{J_1(qc)} \cdot \frac{H_{0,1}(pb, pc)}{H_{0,0}(pb, pc)} + \frac{H_{0,0}(qb, qa)\, H_{1,0}(pb, pc)}{H_{1,0}(qb, qa)\, H_{0,0}(pb, pc)}\right] + 1 \tag{4}$$

for the hollow beam (Fig. VI-6); and

$$D(pb, qb, a, b) = pb\, \frac{J_1(pb)}{J_o(pb)} - qb\, \frac{H_{1,0}(qb, qa)}{H_{0,0}(qb, qa)} \tag{5}$$

for the solid beam. The biradial H-functions (3) are

$$H_{m,n}(x, y) = \frac{\pi}{2}\left[J_m(x)N_n(y)-N_m(x)J_n(y)\right] \tag{6}$$

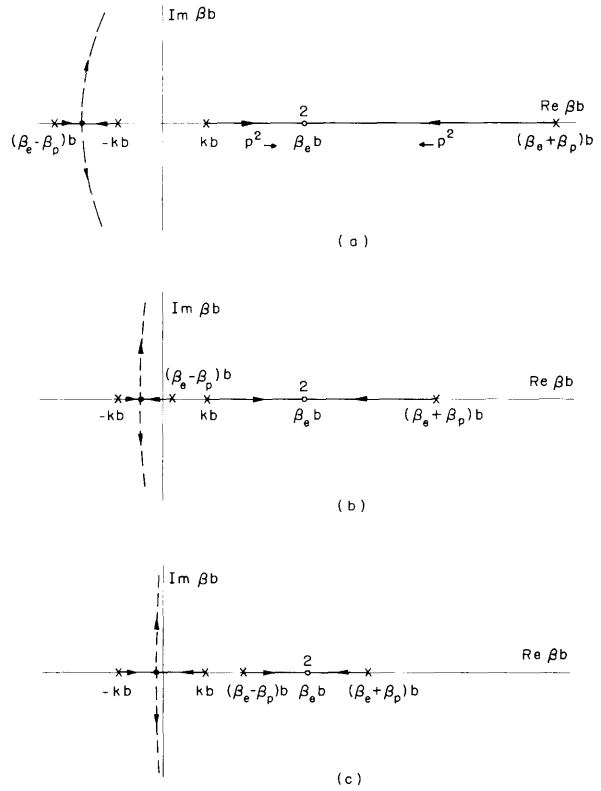

Fig. VI-7. Root locus plots for Eq. 2 with $(pb)^2$ real and positive: (a) $\omega_p/\omega > \left(1 + \frac{v_o}{c}\right)$; (b) $\left(1 - \frac{v_o}{c}\right) < \omega_p/\omega < \left(1 + \frac{v_o}{c}\right)$; (c) $\omega_p/\omega < \left(1 + \frac{v_o}{c}\right)$.

For purely propagating slow waves, $(qb)^2$ must be negative and real. The boundary conditions do not allow $(pb)^2$ to be negative and real when $(qb)^2$ is negative and real, nor can $(pb)^2$ be complex under these conditions. Hence, $(pb)^2$ must be positive and real.

The possible values of βb that satisfy Eq. 2 can be represented graphically with the aid of a root locus diagram. Figure VI-7 shows root locus diagrams for $(pb)^2$ positive and real and with fixed values of $\beta_e b$ and kb, for three different values of $\beta_p b$. The arrows on the loci of Fig. VI-7 show the direction of displacement of the values of βb that satisfy Eq. 2 as $(pb)^2$ is increased. The loci of Fig. VI-7 for complex βb are dotted because the complex βb will not satisfy Eq. 3 when $(pb)^2$ is positive and real. Figure VI-7a shows the condition for which βb is negative, real, and larger than kb. The diagram shows that for backward slow waves to exist $(\beta_e - \beta_p)$ b must be less than -kb (that is, $\omega_p/\omega > 1 + v_o/c$). With this condition satisfied, backward slow waves will exist if the boundary condition equation, Eq. 3, is satisfied simultaneously.

The solution of Eq. 3, for $(pb)^2$ real and positive with $(qb)^2$ real and negative for either the hollow or solid beam, can be presented in the form shown in Fig. VI-8b.

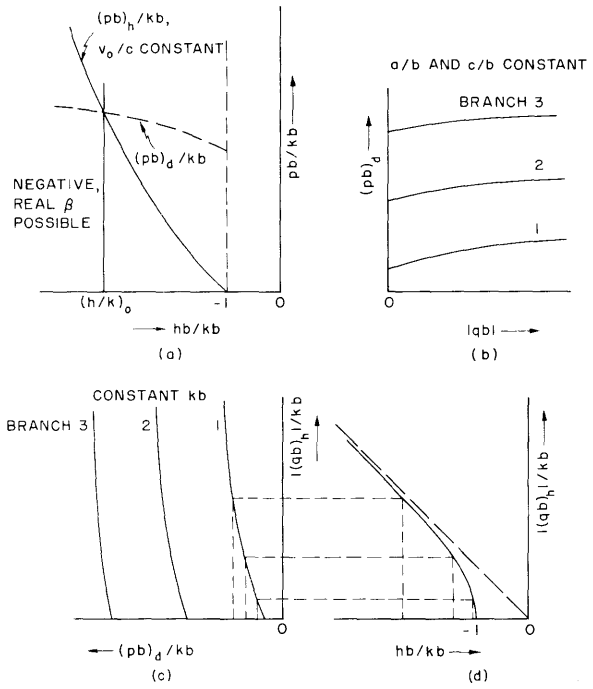

Fig. VI-8. Demonstration of the solution for negative real β when $\omega_p/\omega > \left(1 + \frac{v_o}{c}\right)$.

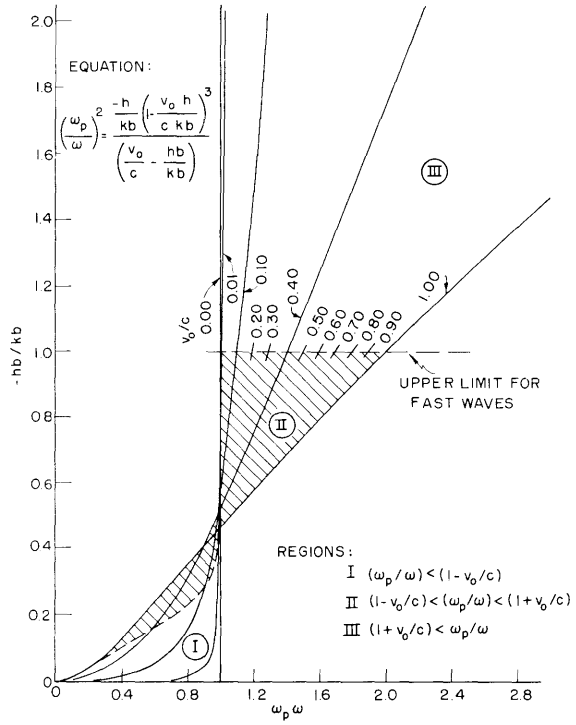

Fig. VI-9. Variation of break point with ω_p/ω and v_o/c for $(pb)^2$ positive and real.

Hereafter, the values of pb that satisfy Eq. 3 will be denoted by $(pb)_d$. The maximum value of $(pb)^2$, from Eq. 2, for which pure real βb are obtained occurs at the break point, where the dotted loci leave the real axis in Fig. VI-7. Let the value of βb at the break point be hb. It can be shown (4) that the break point satisfies the expression

$$\left(\frac{\omega_p}{\omega}\right)^2 = \frac{\frac{hb}{kb}\left(\frac{hb}{kb}\cdot\frac{v_o}{c}-1\right)^3}{\left(\frac{v_o}{c}-\frac{hb}{kb}\right)} \tag{7}$$

Figure VI-9 shows the solution of Eq. 7 with v_o/c as a parameter. The value of $(pb)^2$ at the break point, $(pb)_h$, is found by substituting hb for βb in Eq. 2. Backward slow waves will be possible if $(pb)_h$ exceeds $(pb)_d$ at $\beta b = hb$. (Note that the value of $pb = f(\beta b, kb, \beta_p b, \beta_e b)$ increases from zero as βb decreases from $-kb$, while $(pb)_d$ increases slowly from some positive value at $\beta b = -kb$.)

A method for finding the conditions for which $(pb)_h$ exceeds $(pb)_d$ is demonstrated in Fig. VI-8. Specification of the average drift velocity, v_o/c, gives a particular solution of $(pb)_h = f(hb/kb, v_o/c)$, as indicated by the solid curve of Fig. VI-8a (note that the break point variable is on the abscissa). Specification of beam and drift-tube radii determines $(pb)_d = f(qb, a, b, c)$ from the boundary condition determinantal equations (Fig. VI-8b). With the normalized beam radius, kb, given, $(pb)_d/kb = f(qb/kb, a, b, c)$ and hb/kb may be found (Fig. VI-8c). A functional relationship between $f(qb/kb, a, b, c)$ and hb/kb may be found with the aid of the relation

$$|qb|_h/kb = [(hb/kb)^2-1]^{1/2} \tag{8}$$

Equation 8 is sketched in Fig. VI-8d; and the determination of

$$(pb)_d/kb = f(hb/kb, a, b, c) \tag{9}$$

is indicated in Fig. VI-8c and 8d. The intersection of the normalized boundary condition curve (Eq. 9 shown dashed in Fig. VI-8a) with the break point curve, as shown in Fig. VI-8a, determines the break point $(h/k)_o$ at which negative, real, propagation constants become possible for the given system. Either Fig. VI-9 or Eq. 7 may be used to find the relative plasma frequency (ω_p/ω) for a given break point hb/kb.

When the system parameters are all given, a test for backward slow waves may be made by finding hb/kb from Fig. VI-9, calculating $(pb)_h/kb$ from Eq. 2, and comparing the result with $(pb)_d$, obtained from Eq. 3, with $qh = (qb)_h$. The variation of the break point as a function of v_o/c can be found, once $(pb)_d/kb$ is known.

C. G. Alexander, A. Bers

References

1. W. C. Hahn, Small-signal theory of velocity-modulated electron beams, Gen. Elec. Rev. 42, 258-70 (June 1939).

2. S. Ramo, The electronic-wave theory of velocity-modulation tubes, Proc. IRE 27, 757-763 (1939).

3. C. K. Birdsall, Bi-Radial Functions and Sheath Helix Velocity Curves, Informal Report, General Electric Microwave Laboratory, Palo Alto, California, 1953.

4. G. J. Murphy, Basic Automatic Control Theory (D. Van Nostrand Company, Inc., New York, 1957).

C. ONE-DIMENSIONAL GAP INTERACTION

Consider a one-dimensional electron stream whose motion is constrained (by an infinite magnetic-focusing field) to be only in the z-direction. Let the time-average velocity of the stream be v_o and the time-average charge density be ρ_o. The time-average electron density is neutralized by a stationary ion background. Fields external to this system may exist (either applied or induced by the electron stream) between two infinite parallel plane grids that do not intercept any of the moving charges (see Fig. IV-10). This system is different from the one-dimensional gap system of Llewellyn (1) in that between the planes there is no depression of the time-average potential caused by space charge.

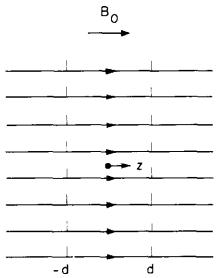

Fig. VI-10. One-dimensional electron stream and gridded gap.

The solution for the interaction between the gap fields and the space-charge fields is a special case of the theory given previously (2, 3). Here, we shall give a numerical evaluation of the parameters in the solution.

For the region between the grids, the linearized Maxwell equation, and the force and continuity equations give

$$\left(j\beta_e + \frac{\partial}{\partial z}\right) V(z) = jZ_o\beta_p\, I(z) + E_z^c(z) \tag{1}$$

$$\left(j\beta_e + \frac{\partial}{\partial z}\right) I(z) = jY_o\beta_p\, V(z) \tag{2}$$

where $\beta_e = \omega/v_o$ is the electron phase constant, $\beta_p = \omega_p/v_o$ is the plasma phase constant, $V(z) = mv_o v(z)/e$ is the kinetic voltage, $E_z^c(z)$ is the electric field resulting from charges

on the grids, $I(z) = \sigma J(z)$ is the beam-current modulation (σ is a particular cross-section area transverse to z) and

$$Y_o = \frac{1}{Z_o} = \omega \epsilon_o \sigma \beta_p = \frac{I_o}{R(R+1)\, V_o} \frac{\omega}{\omega_p} \tag{3}$$

with $R = \left(1+v_o^2/c^2\right)^{-1/2}$; I_o, the time-average beam current; and V_o, the time-average beam voltage. Equations 1, 2, and 3 apply to an electron stream with relativistic time-average velocities. The electron mass m in the definitions of kinetic voltage and of the plasma frequency $\left(\omega_p^2 = m\rho_o/e\epsilon_o\right)$ is the longitudinal mass, $m = m_o R^3$.

The interaction can be conveniently described by the following linear representation

$$\begin{bmatrix} V(z) \\ I(z) \\ \hline I_g \end{bmatrix} = \left[\begin{array}{cc|c} A & B & a \\ C & D & b \\ \hline c & c & Y_{e\ell} \end{array}\right] \begin{bmatrix} V(-d) \\ I(-d) \\ \hline V_g \end{bmatrix} \tag{4}$$

or in matrix form with the partitioning as shown in Eq. 4:

$$\begin{bmatrix} \underline{\underline{B}}_2 \\ \hline I_g \end{bmatrix} = \left[\begin{array}{c|c} \underline{\underline{D}} & \underline{\underline{K}} \\ \hline \underline{\underline{\Gamma}} & Y_{e\ell} \end{array}\right] \begin{bmatrix} \underline{\underline{B}}_1 \\ \hline V_g \end{bmatrix}$$

$$= \left[\begin{array}{c|c} \underline{\underline{D}}_{g2} & \underline{\underline{0}} \\ \hline \underline{\underline{0}} & \underline{\underline{1}} \end{array}\right] \left[\begin{array}{c|c} \underline{\underline{I}} & \underline{\underline{K}}_g \\ \hline \underline{\underline{\Gamma}}_g & Y_{e\ell} \end{array}\right] \left[\begin{array}{c|c} \underline{\underline{D}}_{1g} & \underline{\underline{0}} \\ \hline \underline{\underline{0}} & \underline{\underline{1}} \end{array}\right] \begin{bmatrix} \underline{\underline{B}}_1 \\ \hline V_g \end{bmatrix} \tag{5}$$

The drift matrix $D = D_{g2}D_{1g}$ describes the drifting transformation of the modulations on the beam in the absence of circuit fields between the grids

$$A = D = \frac{1}{2}\left\{\exp[-j\beta_+(d+z)]+\exp[-j\beta_-(d+z)]\right\} = \cos\beta_p(d+z)\exp[-j\beta_e(d+z)] \tag{6}$$

$$B = \frac{1}{2} Z_o\left\{\exp[-j\beta_+(d+z)]-\exp[-j\beta_-(d+z)]\right\} = jZ_o \sin\beta_p(d+z)\exp[-j\beta_e(d+z)] \tag{7}$$

$$C = \frac{1}{2} Y_o\left\{\exp[-j\beta_+(d+z)]-\exp[-j\beta_-(d+z)]\right\} = jY_o \sin\beta_p(d+z)\exp[-j\beta_e(d+z)] \tag{8}$$

where

$$\beta_+ = \beta_e - \beta_p \tag{9}$$

and

$$\beta_- = \beta_e + \beta_p \tag{10}$$

are, respectively, the fast and slow space-charge wave propagation constants of the

natural system of a freely drifting electron stream. The coupling matrices $\underline{\underline{K}}_g$ and $\underline{\underline{\Gamma}}_g$ are given by

$$\underline{\underline{K}}_g = \begin{bmatrix} M \\ Y_o N \end{bmatrix} \tag{11}$$

$$\underline{\underline{\Gamma}}_g = \begin{bmatrix} Y_o N^* & M^* \end{bmatrix} \tag{12}$$

where

$$M = \frac{1}{2}(M_+ + M_-) \tag{13}$$

$$N = \frac{1}{2}(M_+ - M_-) \tag{14}$$

and

$$M_\pm = \int_{-d}^{d} E_z^c(z)\, e^{j\beta_\pm z}\, dz \tag{15}$$

The electronic-loading admittance $Y_{e\ell} = G_{e\ell} + jB_{e\ell}$ is found to be

$$G_{e\ell} = \mathrm{Re}\left(Y_o M N^*\right) = \frac{1}{4} Y_o \left[|M_+|^2 - |M_-|^2 \right] \tag{16}$$

$$B_{e\ell} = \frac{1}{4} Y_o \left[\mathrm{Im}\left(2M_+ M_-^* e^{jz\beta_p d}\right) - \mathrm{Re} \int_{-d}^{d} 4M_+(z)\, M_-(z)\, e^{jz\beta_p z}\, dz \right] \tag{17}$$

Equations 11-17 are for an arbitrary variation of the electric field $E_z^c(z)$ between the grids. For a uniform circuit field

$$\begin{aligned} E_z^c(z) &= \frac{1}{2d} && |z| \leq d \\ &= 0 && |z| \geq d \end{aligned} \tag{18}$$

we have

$$M_\pm = \frac{\sin \beta_\pm d}{\beta_\pm d} \tag{19}$$

from which M and N follow readily. The electronic-loading admittance is found to be

$$G_{e\ell} = \frac{1}{4} Y_o \left[\left(\frac{\sin \beta_+ d}{\beta_+ d} \right)^2 - \left(\frac{\sin \beta_- d}{\beta_- d} \right)^2 \right] \tag{20}$$

$$B_{e\ell} = \frac{1}{4} Y_o \left[\frac{\sin \beta_+ d \cos \beta_+ d - \beta_+ d}{(\beta_+ d)^2} - \frac{\sin \beta_- d \cos \beta_- d - \beta_- d}{(\beta_- d)^2} \right] \tag{21}$$

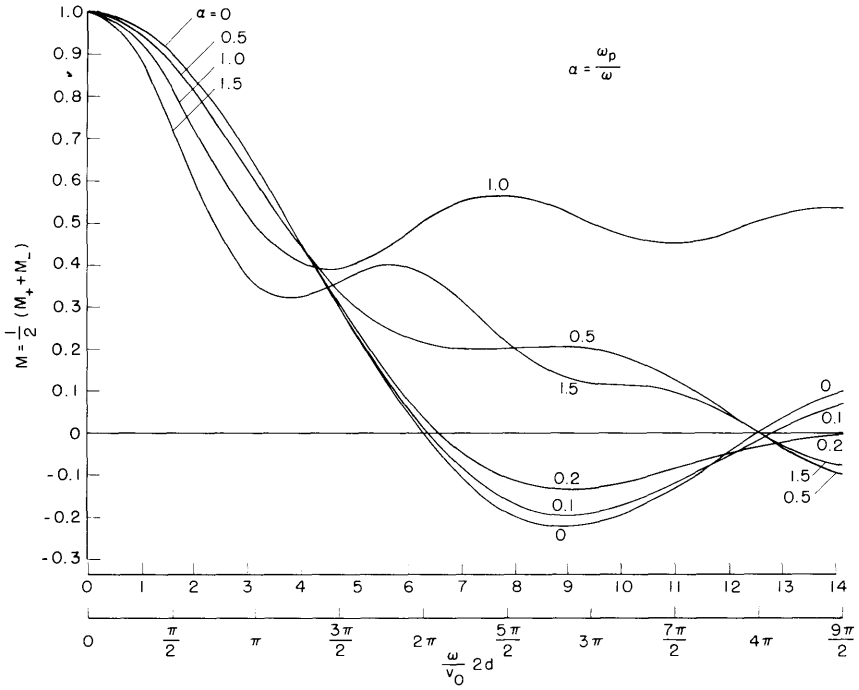

Fig. VI-11. Voltage-gap coupling coefficient.

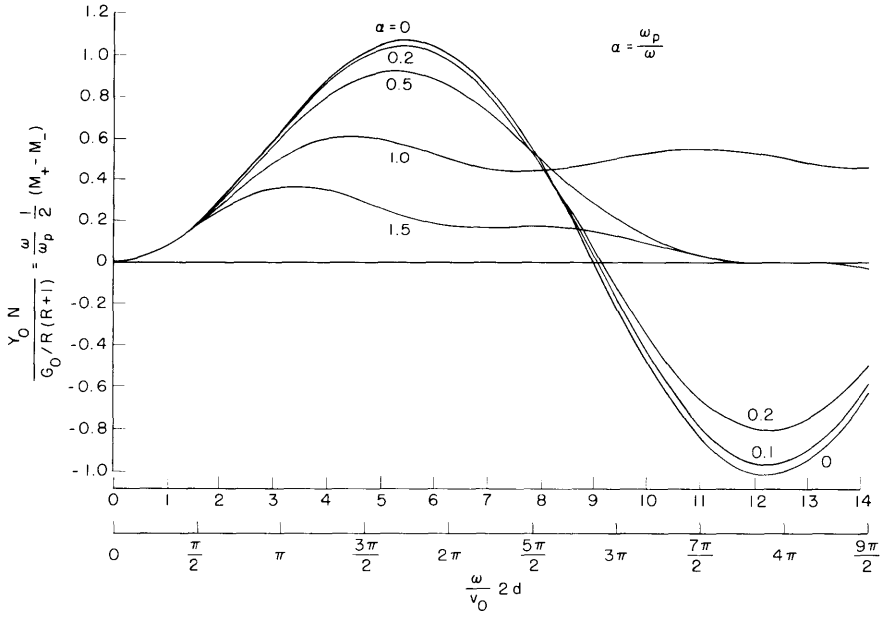

Fig. VI-12. Current-gap coupling coefficient.

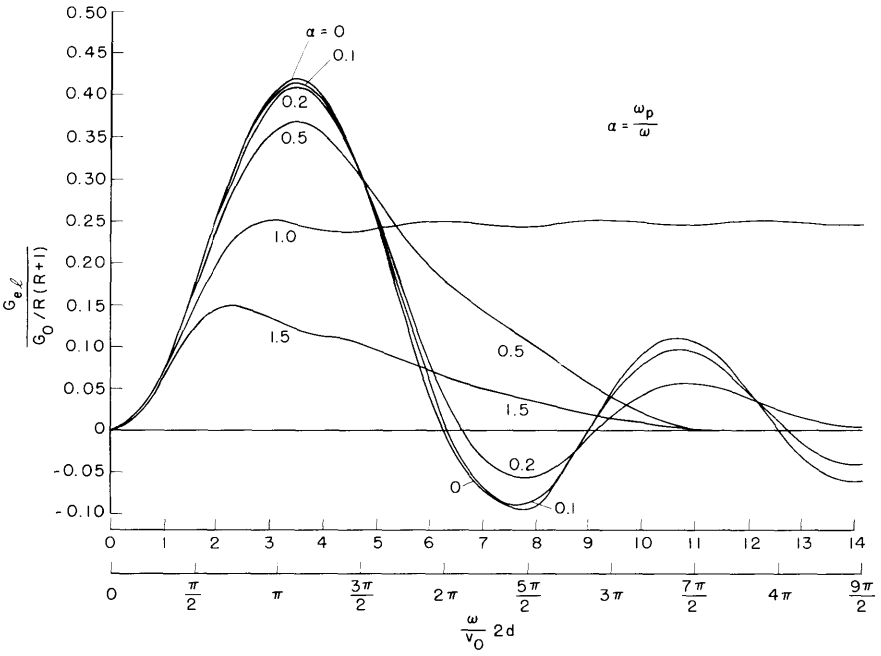

Fig. VI-13. Electronic-loading conductance.

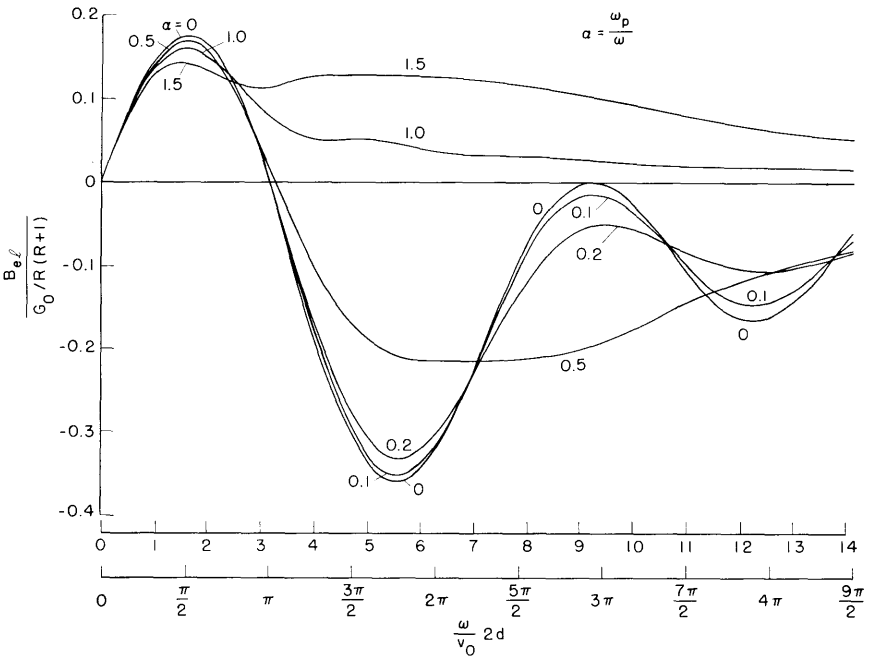

Fig. VI-14. Electronic-loading susceptance.

Figures VI-11, VI-12, VI-13, and VI-14 give the variation of M, $Y_o N$, $G_{e\ell}$, and $B_{e\ell}$, respectively as functions of the normalized gap length $\beta_e 2d$, with the normalized plasma frequency ω_p/ω as a parameter.

A. Bers

References

1. F. B. Llewellyn, Electron Inertia Effects (Cambridge University Press, London, 1941).

2. A. Bers, Interaction of Electrons with Electromagnetic Fields of Gaps with Application to Multicavity Klystrons, Sc. D. Thesis, Department of Electrical Engineering, M. I. T., June 1959.

3. A. Bers, Linear space-charge theory of gap interactions, Quarterly Progress Report No. 52, Research Laboratory of Electronics, M. I. T., Jan. 15, 1959, pp. 39-43.

D. ERRATA

[The author, A. Bers, requests that the following changes be made in his discussions of the space-charge theory of gap interaction that have appeared in our Quarterly Progress Reports. Ed.]

Quarterly Progress Report No. 52, January 15, 1959

Page 41. For the equation below Eq. 12, read:

$$Y_o = \frac{1}{Z_o} = \frac{I_o}{R(R+1)\,V_o}\,\frac{\omega}{\omega_q}; \qquad R = \left[1 - \frac{v_o^2}{c^2}\right]^{-1/2}$$

Quarterly Progress Report No. 55, October 15, 1959

Page 66. For Eq. 2, read:

$$\begin{bmatrix} \underline{\underline{B}}_2 \\ \hline I_g \end{bmatrix} = \left[\begin{array}{c|c} \underline{\underline{D}}\ F(pr) & \underline{\underline{K}}\ F(pr) \\ \hline \underline{\underline{\Gamma}} & Y_{e\ell} \end{array}\right] \begin{bmatrix} \underline{\underline{B}}_1 \\ \hline V_g \end{bmatrix}$$

Page 66. For the last term in the equation below Eq. 5, read:

$$\left(k = \frac{\omega}{c}\right)$$

Page 67. For Eq. 12, read:

$$Y_{on} = \frac{I_o}{R(R+1)\,V_o}\,\frac{\omega}{\omega_{qn}}; \qquad R = \left[1 - \frac{v_o^2}{c^2}\right]^{-1/2}$$

Page 68. For Eq. 24, read:

$$C_n E_c(z) = \frac{\int_\sigma E_c(z, r)\, J_o(p_n r)\, da}{\int_\sigma J_o^2(p_n r)\, da}$$

Page 68. For Eq. 25, read:

$$C_B E_c(z) = E_c(z, b)$$

Page 68. For the equation below Eq. 25, read:

$$E_c(z, r) = \frac{1}{2\pi} \int_{-\infty}^{\infty} \frac{J_o(vr)}{J_o(va)}\, M(u)\, e^{-juz}\, du$$

$$v^2 = -u^2 + k^2$$

Page 68. For Eqs. 27, 28, and 29, read:

$$a_{n, B} = \frac{1}{2} \left[M_{+n, B} C_{+n, B} \exp(-j\beta_{+n, B}) + M_{-n, B} C_{-n, B} \exp(-j\beta_{-n, B} z)\right]$$

$$b_{n, B} = \frac{1}{2} Y_{on, B} \left[M_{+n, B} C_{+n, B} \exp(-j\beta_{+n, B} z) - M_{-n, B} C_{-n, B} \exp(-j\beta_{-n, B} z)\right]$$

$$M_{\pm n, B} = \int_{-\infty}^{\infty} E_c(z, a) \exp(j\beta_{\pm n, B} z)\, dz$$

with

$$C_{\pm n} = \frac{\int_\sigma \frac{J_o(v_{\pm n} r)}{J_o(v_{\pm n} a)}\, J_o(p_n r)\, da}{\int_\sigma J_o^2(p_n r)\, da}$$

$$C_{\pm B} = \frac{J_o(v_{\pm B} b)}{J_o(v_{\pm B} a)}$$

$$v_{\pm n, B}^2 = -\beta_{\pm n, B}^2 + k^2$$

Page 69. For Eq. 32, read:

$$c_{n, B} = \frac{1}{2} Y_{on, B} \left[M_{+n, B}^* K_{+n, B} \exp(-j\beta_{+n, B} \ell) - M_{-n, B}^* K_{-n, B} \exp(-j\beta_{-n, B} \ell)\right]$$

Page 69. For Eq. 33, read:

$$d_{n,B} = \frac{1}{2}\left[M^*_{+n,B}K_{+n,B}\exp(-j\beta_{+n,B}\ell) + M^*_{-n,B}K_{-n,B}\exp(-j\beta_{-n,B}\ell)\right]$$

Page 69. For Eq. 34, read:

$$K_{\pm n} = C_{\pm n}\frac{1}{\sigma}\int_{\sigma} J_o^2(p_n r)\,da$$

Page 69. For Eq. 35, read:

$$K_{\pm B} = C_{\pm B}$$

Page 69. For Eq. 36, read:

$$G_{e\ell n,B} = \frac{1}{4}Y_{on,B}\left[|M_{+n,B}|^2 C_{+n,B}K_{+n,B} - |M_{-n,B}|^2 C_{-n,B}K_{-n,B}\right]$$

Page 69. For Eq. 38, read:

$$B_{e\ell n,B} = \frac{1}{4}Y_{on,B}\,\mathrm{Im}\left[2M_+K_+M_-^*K_-\exp(j2\beta_{qn,B}\ell)\right] - 4\omega\left(W_k - W_e^p\right)_{V_g=1}$$

where

$$W_k = \frac{1}{4}\epsilon_o\int_{\sigma} da\int dz\,|\beta_p a(z)|^2 J_o^2(pr)$$

and

$$W_e^p = \frac{1}{4}\epsilon_o\int_{\sigma} da\int dz\left|\frac{D}{Dz}a(z)J_o(pr) - E_z^c(z,r)\right|^2$$

Quarterly Progress Report No. 56, January 15, 1960

Page 98. For Eq. 1, read:

$$\begin{bmatrix}\underline{\underline{B}}_{II}\\ I_g\end{bmatrix} = \left[\begin{array}{c|c}\underline{\underline{D}}_{I,II}F(r) & D_{gII}\,\underline{\underline{K}}_g F(r)\\ \hline \underline{\underline{\Gamma}}_g\,\underline{\underline{D}}_{Ig} & Y_{e\ell}\end{array}\right]\begin{bmatrix}\underline{\underline{B}}_I\\ V_g\end{bmatrix}$$

Page 98. For Eq. 5, read:

$$M_k = \frac{1}{2}\left[M_{+k}C_{+k} + M_{-k}C_{-k}\right]$$

Page 100. For Eq. 6, read:

$$N_k = \frac{1}{2}\left[M_{+k}C_{+k} - M_{-k}C_{-k}\right]$$

Page 100. For Eq. 8, read:

$$M_k' = \frac{1}{2}\left[M^*_{+k}K_{+k} + M^*_{-k}K_{-k}\right]$$

Page 100. For Eq. 9, read:

$$N'_k = \frac{1}{2}\left[M^*_{+k}K_{+k} - M^*_{-k}K_{-k}\right]$$

Page 100. For Eq. 10, read:

$$\begin{bmatrix} \underline{\underline{B}}_I \\ I_g \end{bmatrix} = \left[\begin{array}{c|c} \underline{\underline{D}}_{gII}F(r) & \underline{\underline{0}} \\ \hline \underline{\underline{0}} & 1 \end{array}\right]\left[\begin{array}{c|c} \underline{\underline{I}} & \underline{\underline{K}}_g \\ \hline \underline{\underline{\Gamma}}_g & Y_{e\ell} \end{array}\right]\left[\begin{array}{c|c} \underline{\underline{D}}_{Ig} & \underline{\underline{0}} \\ \hline \underline{\underline{0}} & 1 \end{array}\right]$$

Page 100. For Eq. 12, read:

$$G_{e\ell} = \frac{1}{4}\sum_k Y_{ok}\left[|M_{+k}|^2 C_{+k}K_{+k} - |M_{-k}|^2 C_{-k}K_{-k}\right]$$

E. TRANSMISSION ZEROS OF THE FOUR-CAVITY KLYSTRON

The transfer impedance (defined here as the ratio of the output gap voltage to the input gap source current) of the four-cavity klystron (1) can be expressed as

$$\frac{V_{g4}}{I_{s1}} = y_{41}Z_4Z_1T_4 \tag{1}$$

$$T_4 = 1 + \frac{y_{42}y_{21}}{y_{41}}Z_2 + \frac{y_{43}y_{31}}{y_{41}}Z_3 + \frac{y_{43}y_{32}y_{21}}{y_{41}}Z_2Z_3 \tag{2}$$

where Z_k is the impedance of the k^{th} cavity and y_{kj} is the klystron transconductance between identical gaps j and k.

$$y_{kj} = 2G_{e\ell}\left[\cos\theta_{kj} + j\frac{M^2Y_o}{2G_{e\ell}}\sin\theta_{kj}\right]\exp(-j\theta_e)_{kj} \tag{3}$$

If we use the narrow-band approximation for the cavity impedance, the transmission function of Eq. 2 becomes the ratio of two second-degree polynomials. In the examples given below, a shift of origin and a normalization have been introduced; the (R/Q) ratios and the real part of the poles, α, of the second and third cavities are assumed to be equal. Thus the poles of the transmission function are located at $-\alpha \pm j1$. The position of the zeros is then determined by the values of the gap factor $a = Y_oM^2/2G_{e\ell}$, the center-gap to center-gap drift lengths, $\theta_{kj} = (2\pi\ell/\lambda_q)$, the external loading factor $b = G_{e\ell}/(G_c+G_{e\ell})$, gain per stage $g = 2ab$, and the position of the poles (2).

EXAMPLE 1: Figures VI-15 and VI-16 show the loci of the transmission zeros for an equal drift length klystron with a two-pole Butterworth distribution (α=1). Klystron A

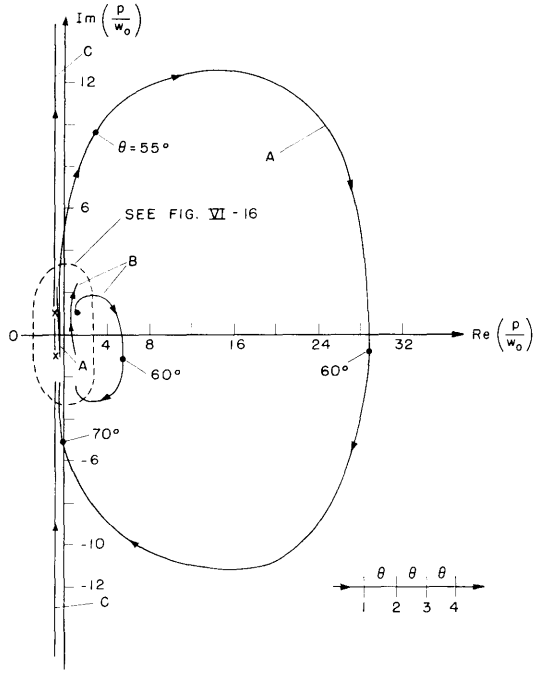

Fig. VI-15. Equal drift length loci (Example 1).

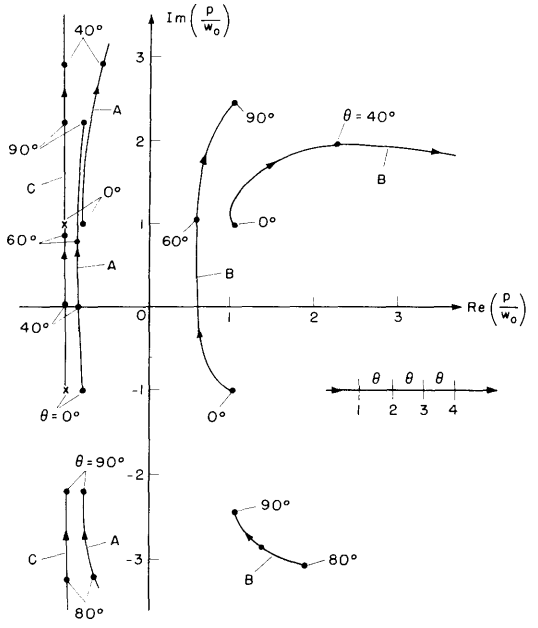

Fig. VI-16. Enlargement of loci near the origin (Example 1).

(a=10, b=0.1, g=2) is a short-gap klystron with low electronic loading. Klystron B (a=1.5, b=1, g=3) is a long-gap klystron with large electronic loading. Klystron C (a=∞, b=0, g=2) is the limiting case of a klystron having gaps of zero length and zero electronic loading. The loci of klystron C are based on the commonly used approximate description of gap interaction (3). These loci are to be compared with those of klystrons A and B, which are based on a complete description of gap interaction that properly accounts for electronic loading and remodulations of both kinetic voltage and beam current.

Examination of Figs. IV-15 and IV-16 reveals the following trends: (a) The area of the loci increases as the gap factor a is increased. (b) The value of the external-loading factor b largely determines whether or not the loci will enter the left half-plane. For large values (near unity) of b, the loci lie entirely in the right half-plane. (c) The zero loci of klystron A follow the loci of klystron C fairly closely, except when θ_{41} approaches 180°. At this point, one zero of klystron C goes to infinity, while the zero of klystron A moves far out of the passband into the right half-plane, but remains at a finite distance from the passband. Note that a zero far out in the right half-plane represents a large, nearly constant multiplier of the power-gain function throughout the passband. (d) Each zero may be associated with a particular pole — that pole which is directly opposite the zero at θ = 0°. The zero associated with the low-frequency pole moves upward out of the passband as θ increases. Its real part decreases slightly and then increases to its original value. The zero associated with the high-frequency pole moves in a large clockwise quasi circle.

EXAMPLE 2: For this example we have again assumed equal drift lengths, and a

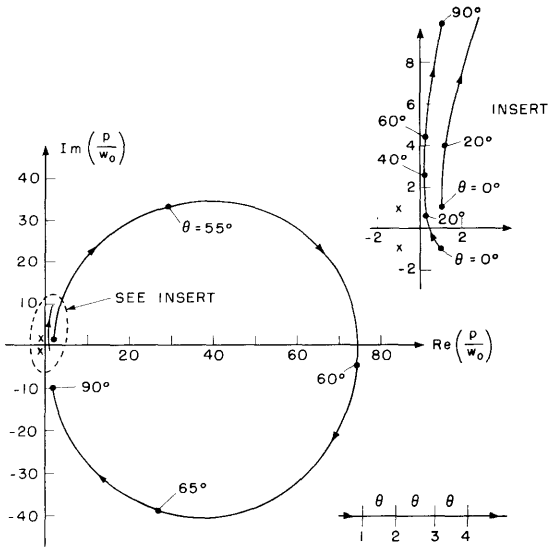

Fig. VI-17. Equal drift length loci (Example 2).

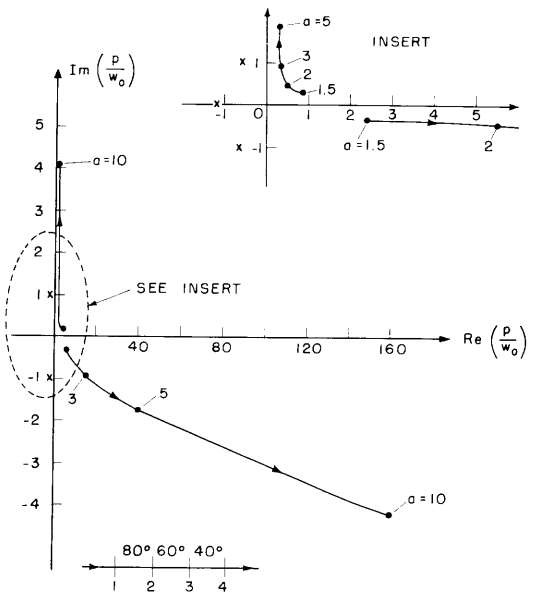

Fig. IV-18. Locus for 80°-60°-40° klystron with variable gap factor, a (Example 3).

Butterworth pole distribution for the second and third cavities. The gap factor is 5; the electronic loading is large, b = 1; the gain per stage is 10. Figure IV-17 shows that the loci are quite similar to those of Example 1. However, the zeros have moved farther out of the passband at $\theta = 90°$. This difference may be attributed to the fact that the gain per stage is much higher.

EXAMPLE 3: The pole positions have been chosen so as to produce a maximally flat response (in the absence of zeros) with the first three cavities, $a = 1/\sqrt{3}$. The electronic loading is large, b = 1, and the output cavity is assumed to have a bandwidth equal to or larger than the over-all tube bandwidth. This requirement on the output cavity is common in high-power klystrons for achieving efficient power transfer to the load over the passband. The drift lengths decrease in the direction of motion of the electron beam: $\theta_{12} = 80°$, $\theta_{23} = 60°$, $\theta_{34} = 40°$. Thus the klystron of this example should be a good approximation to a high-power klystron. Figure VI-18 gives the zero loci as a function of the gap factor. We can see that increasing the gap factor shifts the zeros farther away from the passband. Thus for a given set of drift lengths, the largest gain will be obtained by making the gap factor as large as possible.

R. H. McCullough, A. Bers

References

1. A. Bers, Interaction of Electrons with Electromagnetic Fields of Gaps with Application to Multicavity Klystrons, Sc. D. Thesis, Department of Electrical Engineering, M. I. T., June 1959.

2. R. H. McCullough, Network Characteristics of the Multicavity Klystron, S. M. Thesis, Department of Electrical Engineering, M. I. T., September 1960.

3. K. H. Kreuchen, B. A. Auld, and N. E. Dixon, A study of the broadband frequency response of the multicavity klystron, J. Electronics, 2, 529 (1957).